

Supporting Information

A Novel S-Scheme Heterojunction Constructed by Ti-Based Hydrotalcite Decorating MOFs for Boosting CO₂-to-CO Photoreduction and Mechanism Insight

*Ruonan Wang^a, Zhen Wang^b, Xiaofang Shang^a, Yan Yang^a, Jie Ding^{a, *}, Qin Zhong^{a, *}.*

^a School of Chemistry and Chemical Engineering, Nanjing University of Science and Technology,
Nanjing, Jiangsu 210094, PR China

^b Key Laboratory of Coal Science and Technology, Ministry of Education and Shanxi Province,
Taiyuan University of Technology, Taiyuan 030024, Shanxi, China

* Corresponding Author: Qin Zhong e-mail: zq304@njjust.edu.cn;

Jie Ding e-mail: tonlyjding@njjust.edu.cn.

Contents

S1. Preparation of photocatalysts

S2. Characterizations

S3. Calculation process of CO and CH₄ production rates.

S4. Calculation process of apparent quantum yield (AQY %)

Table S1 Photocatalytic performance over as-prepared photocatalysts.

Table S2 Comparison of photocatalysts toward photocatalytic CO₂ reduction.

Table S3 Band structures for NTL and NM.

Table S4 Fitted parameters from TRPL decays spectra of NM and NM₃NTL₁.

Table S5 Specific surface area and pore structure of as-prepared catalysts.

Figure S1 Zeta potentials of (A) NTL, (B) NM and (C) NM₃NTL₁.

Figure S2 (A) XRD patterns and (B) the partial enlarged details of the as-prepared samples.

Figure S3 FTIR spectra of the as-prepared samples.

Figure S4 SEM of MIL-125.

Figure S5 TEM of NMNTL.

Figure S6 EDX of NM₃NTL₁.

Figure S7 Gas chromatography of reaction gas over NM₃NTL₁ and the pure CO₂ (A), CH₃OH (B), H₂ (C); (D) ion chromatography of reaction and HCOOH.

Figure S8 Mass spectra of CO (A) or CO₂ (B) mixing with H₂O¹⁸.

Figure S9. Photocatalytic activity in the presence of TEOA.

Figure S10 Photocatalytic activity under various pH values.

Figure S11 Recycle experiments of (A) NTL, (B) NM and (C) NM₃NTL₁.

Figure S12 FTIR spectra of fresh and used (A) NTL, (B) NM and (C) NM₃NTL₁.

Figure S13 XRD patterns of fresh and used (A) NTL, (B) NM and (C) NM₃NTL₁.

Figure S14 UV-vis DRS spectra of the NM_xNTL_y samples.

Figure S15 Wide scan of XPS spectra.

Figure S16 (A) AFM image of NM₃NTL₁ composite; (B) the corresponding surface potential curves correspond to the KPFM potential image in Figure 5 (B).

Figure S17 EPR results of (A) DMPO-·OH, (B) DMPO-·O₂⁻ for NTL, NM and NMNTL after irradiation for 5 min.

Figure S18 (A) EIS Nyquist plots; (B) Photoluminescence spectra of photocatalysts.

Figure S19 (A) N₂ adsorption-desorption isotherms and (B) the corresponding BJH mesopore size distributions.

Figure S20 TG analysis of (A) NM and (B) NTL.

Figure S21 CO₂-TPD analysis of NM, NTL and NMNTL.

Figure S22 CO₂ pulse adsorption of as-prepared samples.

Figure S23 In situ DRIFTS measurement for NM.

Figure S24 Contact angle for NM with H₂O.

Figure S25 Gas chromatography of reaction gas and the pure CO₂.

Figure S26 O₂ pulse adsorption of NM.

Figure S27 CO oxidation mechanism.

S1 Preparation of photocatalysts

S1.1 Preparation of MIL-125 and NM

MIL-125 was synthesized referencing a previous report with some modifications ^[1]. In detail, 2.04 g tetrabutyl titanate and 1.00 g H₂BDC were dissolved in 72 mL DMF and 8 mL CH₃OH. The mixture was stirred for 30 min at 30 °C to achieve homogeneous solution. Then, the solution was heated to 150 °C in a Teflon autoclave and maintain for 20 h. Subsequently, the MIL-125 was obtained by centrifugating, washing and drying under 80 °C in an oven overnight.

The NM was prepared by the similar pathway as MIL-125. Briefly, a mixture of 2.04 g tetrabutyl titanate, 4.35 g NH₂-H₂BDC, 72 mL DMF and 8 mL CH₃OH was stirred for 30 min at first. Then, the solution was heated at 150 °C for 72 h. Eventually, through centrifugation, washing and drying process, the yellow powder NM was collected. The preparation route was exhibited in **Figure 1**.

S1.2 Preparation of NTL

NTL was prepared by the following process: First, 1.45 g Ni(NO₃)₂·6H₂O, 0.57 g tetrabutyl titanate and 1.1 g urea were mixed with 100 mL H₂O and 1 mL ethanol. Then, the solution was stirred at 100 °C for 24 h in a beaker. Afterwards, NTL was obtained after centrifuging, washing and drying in an oven overnight as shown in **Figure 1**.

S2. Characterizations

S2.1. Structure and morphology characterizations

X-ray diffraction (XRD) test was conducted on a Bruker D2 PHASER system under 36 kV and 30 mA with a Cu K α radiation. The data was collected from 5° to 80° at a scanning rate of 8°/min. Fouriertransform infrared (FTIR, Nicolet IZ10) was measured by potassium bromide tablet method. The morphology was analyzed via transmission electron microscope (TEM, Tecnai

G2 F30) and scanning electron microscopy (SEM, Hitachi S4700). For TEM, the sample was ultrasonically dispersed in ethanol for 10 minutes, and the supernatant was dropped on a copper screen, and dried for characterization. As for SEM, the powder samples were smeared on conducting resin for analyzing. The texture structure of catalysts was determined by N₂ adsorption-desorption apparatus (Micromeritics ASAP 2460). The surface areas of the samples were calculated by Brunauer-Emmett-Teller (BET) method. The pore structure was analyzed by Barrett-Joyner-Halenda (BJH) method. Thermogravimetry (TG) was conducted on a Mettler Toledo 851e thermobalance system at temperature range of 50-600 °C with heating rate of 10 °C min⁻¹. Surface wettability was measured using a static contact angle analyzer (Phoenix 300). Zeta potentials was detected by Malvern Zeta Nano ZS in methanol.

S2.2. Band structure characterizations

Ultraviolet-visible diffuse reflectance spectroscopy (UV-vis DRS) were conducted on a Shimadzu UV-2600 spectrophotometer with a wavelength range of 220–800 nm using BaSO₄ as the reference. The band gaps of photocatalysts were obtained by Tauc's equation:

$$(\alpha h\nu)^n = a_0 (h\nu - E_g) \quad (1)$$

where “ α ” is absorption coefficient; “ $h\nu$ ” is the incident photon energy; “ a_0 ” is an energy independent constant; “ E_g ” is the bandgap energy; “ n ” is determined by the transfer characteristics of electrons in a semiconductor (“ n ” is 2.0 and 0.5 for direct allowed transition and indirect allowed transition, respectively).

X-ray photoelectron spectroscopy (XPS) tests of the catalysts were performed on a Thermo ESCALAB 250 spectrometer with a mono-chromated Al K-alpha source with a power of 150 W. For in-situ irradiated XPS (ISIXPS), a 300 W Xe arc lamp was irradiated and placed ca. 20 cm

away from the photocatalyst for inspecting the variation of electron density under irradiating.

Kelvin probe force microscopy (KPFM, SPM-9700) was used to determine the contact potential difference (CPD) between a conductive probe and samples and subsequently to give the work function of samples. The photo-irradiated KPFM was applied to test the variation of surface potential under dark and irradiation.

Electron spin resonance (EPR) was carried out on a Jeol/JES-FA200 to study the electron transfer mechanism. Specifically, 20 μL of 5,5-dimethyl-1-pyrroline N-oxide (DMPO) with 10 mg of photocatalyst was added to 0.5 mL of distilled water/methanol for testing.

S2.3. Photoelectrochemical characterizations

Electrochemical impedance spectroscopy (EIS), photocurrent and Mott-Schottky measurements were performed on a CHI 760E electrochemical workstation with a three-electrode system. Pt plate and Ag/AgCl electrode were served as the counter electrode and the reference electrode, respectively. A 0.5 mol L⁻¹ Na₂SO₄ solution was used as the electrolyte. The working electrode was prepared as follows: 5 mg catalyst was dissolved in solution containing 30 μL Nafion and 1 mL ethanol. After ultrasonically scattering for 1 h, the slurry was dip-coated onto a FTO glass (1 cm \times 1 cm) and dried at 80 $^{\circ}\text{C}$ for 5 h under a vacuum atmosphere. All the experiments were conducted under a 300 W Xe irradiation.

Photoluminescence (PL) spectra at room temperature were collected using a Labram-HR800-type spectrophotometer. The time-resolved photoluminescence (TRPL) spectra were recorded on the same instrument. The decay curves were fitted using a triexponential decay kinetic:

$$y = y_0 + A_1e^{-x/\tau_1} + A_2e^{-x/\tau_2} \quad (2)$$

and the average PL life times (τ) were calculated according to the following the equation below:

$$\tau = (A_1\tau_1^2 + A_2\tau_2^2) / (A_1\tau_1 + A_2\tau_2) \quad (3)$$

where A_1 and A_2 are constants and related to the nonradiative and radiative relaxation processes, respectively. Besides, τ_1 and τ_2 are relevant to the nonradiative relaxation process and radiative process of direct recombination of carriers, respectively.

S2.4. Surface adsorption and activation characterizations

O₂-temperature programmed desorption (O₂-TPD) was conducted on an AutoChem II 2920 apparatus instrument (Micromeritics, America) coupled with a in-situ mass spectrum (Hidden) using 0.1 g photocatalysts. The samples were pre-treated at 120 °C for 60 min in high-purity helium and then saturated with 2% O₂/Ar for 60 min at 50 °C. Afterwards, these samples were purged with He until excessive O₂ was removed. Then, the TPD data were collected from 50 °C to 120 °C at a ramping rate of 10 °C min⁻¹ in He flow.

CO₂- and O₂- pulse chemisorption experiments were used to determine the CO₂ or O₂ adsorption rates upon catalysts. Prior to experiments, He (10 mL min⁻¹) passed through the photocatalysts at 120 °C for 60 min to remove surface impurity. Subsequently, CO₂/He or O₂/He mixtures with the flow rate of 1 mL min⁻¹ were adsorbed by photocatalysts at 80 °C.

In-situ DRIFT experiments were performed on a Nicolet IZ10 spectrometer equipped with a Harrick Scientific DRIFT cell. Prior to test, photocatalysts were pretreated at 120 °C under N₂ flow (20 mL min⁻¹) for 60 min and then cooled to 40 °C to get the background spectrum. After N₂ flow stopping, CO₂ (20 mL min⁻¹) with bubbled H₂O was introduced into the chamber at 60 °C and reacted at dark for 40 min. Then, the light source was turned on to monitor the produced intermediates for another 30 min.

S3. Calculation process of CO and CH₄ production rates

The CO and CH₄ production rates were calculated as following method.

Firstly, 1mL 0.505% CO calibrating gas was detected and quantified online by a gas chromatograph, gaining an area ($A_{0.505\% \text{ CO}}$). Then, 1 mL produced gas after photocatalytic reaction was injected into a gas chromatograph and gained another area (A_{CO}). Finally, the CO production rates can be calculated by the following Eqs:

$$\text{CO yield} = (P_{\text{CO}} * V_{\text{CO}} * A_{\text{CO}} * n_0 * 0.505\%) / (P_0 * A_{0.505\% \text{ CO}} * T * m) \quad (4)$$

Where “ P_{CO} ” is the pressure at the outlet of the reactor; “ V_{CO} ” is the volume of reactor; “ n_0 ” is the total number of molecules in 1 mL of gas, which is easy obtained by the formula of $PV = nRT$; “ P_0 ” is standard atmospheric pressure; “ T ” is the time of reaction; “ m ” is the dosage of photocatalysts.

S4. Calculation process of apparent quantum yield (AQY %)

The apparent quantum yield (AQY %) is defined as the ratio of number of reacted electrons to the number of incident photons. The apparent quantum yield (AQY %) was calculated based on the equation below.

$$AQY_{\text{CO}}(\%) = \frac{2 \times N_a \times [\text{CO}]}{I \times A \times \frac{\lambda}{hc} \times t} \times 100\% \quad (5)$$

where, [CO] was number of CO (mole) evolved in time “ t ” and N_a was Avogadro’s number ($N_a = 6.022 \times 10^{23} \text{ mol}^{-1}$); I was the incident solar irradiance over the exposed irradiated area A (20.1 cm^2); λ was the wavelength (380, 420, 450, 500 and 550 nm); h was Planck's constant ($6.62 \times 10^{-34} \text{ Js}$) and c was the speed of light ($3.0 \times 10^8 \text{ ms}^{-1}$).

Table S1. Photocatalytic performance over as-prepared photocatalysts.

Catalysts	Formation rate ($\mu\text{mol g}^{-1} \text{h}^{-1}$)		Total electron yield ($\mu\text{mol g}^{-1} \text{h}^{-1}$)
	CO	CH ₄	
MIL-125	5.18	0.29	12.68
NM	9.62	0.26	21.32
NTL	8.12	0.29	18.56
NM ₂ NTL ₁	24.00	0.92	55.36
NM ₃ NTL ₁	28.39	1.12	65.74
NM ₄ NTL ₁	21.34	0.68	48.12

Table S2. Comparison of photocatalysts toward photocatalytic CO₂ reduction.

Catalysts	Products ($\mu\text{mol g}^{-1} \text{h}^{-1}$)	Reaction conditions	Ref.
NH ₂ -MIL-125(Ti) {111}	CO: 8.25; CH ₄ : 1.01	H ₂ O, TEOA, 300 W Xe lamp	[2]
NH ₂ -MIL-125(Ti) {110}/{111}	CO: 15.49; CH ₄ : 5.46	H ₂ O, TEOA, 300 W Xe lamp	[3]
g-C ₃ N ₄ -RGO-NH ₂ -MIL-125(Ti)	CO: 95.94; CH ₄ : 3.45	H ₂ O, 35 W HID Xe lamp	[4]
0.75Ni/Ti-MOFs	CO: 13.37; CH ₄ : 0.35	H ₂ O, TEOA, 300 W Xe lamp	[5]
Cu SAs/UiO-66-NH ₂	CH ₃ OH: 5.33	H ₂ O, TEOA, 300 W Xe lamp	[6]
UiO-66-NH ₂ /RGO-3	CO: 23.54	H ₂ O, TEOA, 300 W Xe lamp	[7]
NiAl-LDH	CO 6.72; CH ₄ , 0.61	H ₂ O, 300 W Xe lamp	[8]
ZnAl-LDH	CO, 7.6	H ₂ O, 500 W Xe lamp	[9]
TiMgAl-LDH/GO	CO, 4.6; CH ₄ , 3.8	H ₂ O, 300 W Xe lamp	[10]

TiO ₂ @Co-Al LDH	CO, 2.21	H ₂ O, 300 W Xe light	[11]
CoZnAl-LDH/RGO/g-C ₃ N ₄	CO, 10.11	H ₂ O, 300 W Xe light	[12]
g-C ₃ N ₄ /NiAl-LDH	CO, 8.2	H ₂ O vapor, 300 W Xe lamp	[13]
FeWO ₄ /NiAl-LDH	CO, 5.0	H ₂ O, 300 W Xe light	[14]
NiAl-LDH/Ti ₃ C ₂	CO, 11.82	H ₂ O, 300 W Xe light	[15]
NM ₃ NTL ₁	CO, 28.39; CH ₄ , 1.12	H ₂ O, 300 W Xe light	This work

Table S3. Band structures for NTL and NM.

Samples	E _g	E _{CB}	E _{VB}
NM	2.80	-0.62	2.18
NTL	2.85	-1.85	1.00

Table S4. Fitted parameters from TRPL decays spectra of NM and NM₃NTL₁.

Photocatalyst	τ_1 /ns	τ_1 /Rel. %	τ_2 /ns	τ_2 /Rel. %	τ /ns
NM	3.63	70.70	14.41	29.30	10.33
NM ₃ NTL ₁	5.71	68.76	23.37	31.24	17.19

Table S5. Specific surface area and pore structure of as-prepared catalysts.

Samples	Surface area (m ² g ⁻¹)	Pore Size (nm)	Pore Volume (m ² g ⁻¹)
NTL	221.79	3.72	0.13
NM ₃ NTL ₁	500.05	4.97	0.10
NM	591.42	5.59	0.097

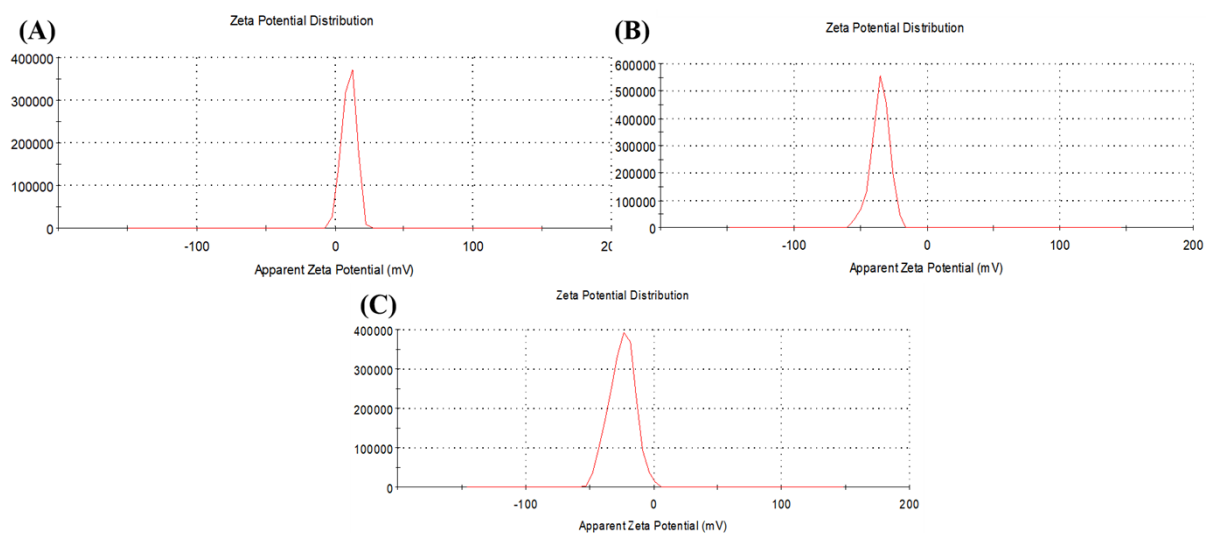


Figure S1 Zeta potentials of (A) NTL, (B) NM and (C) NM₃N TL₁.

Figure S2 (A) XRD patterns and (B) the partial enlarged details of the as-prepared samples.

Figure S3 FTIR spectra of the as-prepared samples.

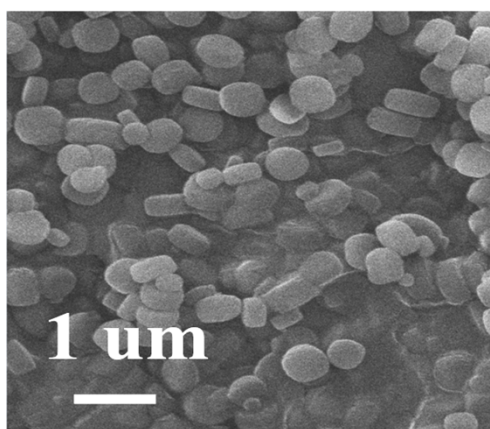


Figure S4 SEM of MIL-125.

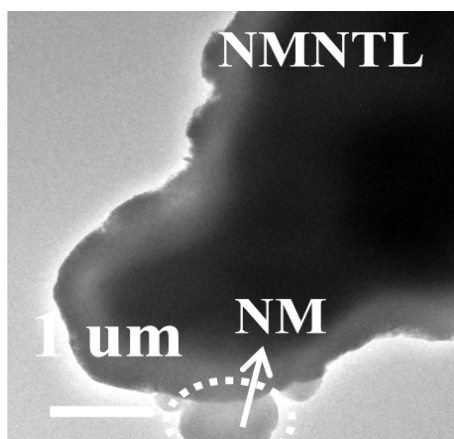


Figure S5 TEM of NMNTL.

Figure S6 EDX of NM_3NTL_1 .

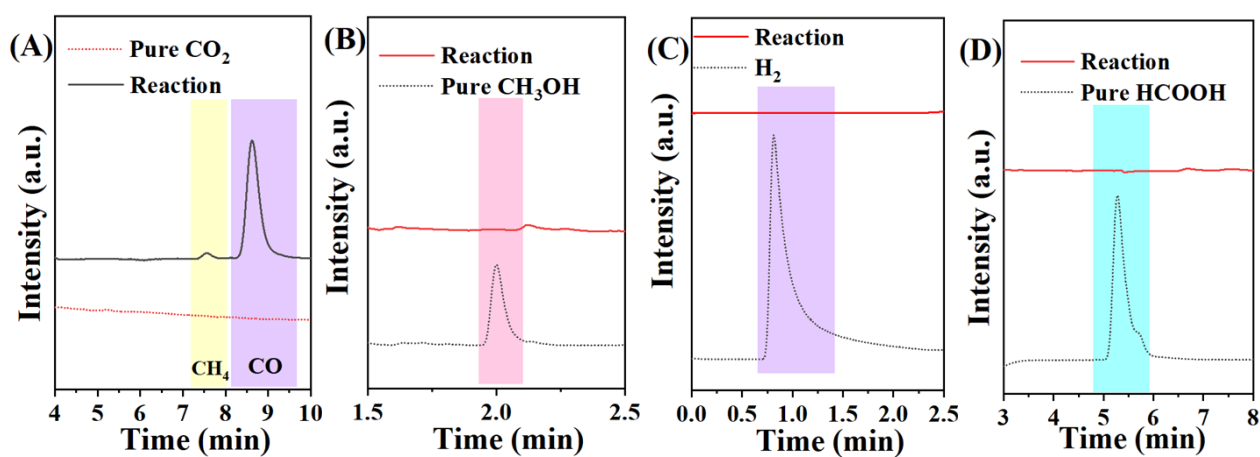


Figure S7 Gas chromatography of reaction gas over NM_3NTL_1 and the pure CO_2 (A), CH_3OH (B), H_2 (C); (D) ion chromatography of reaction and HCOOH .

Figure S8 Mass spectra of CO (A) or CO_2 (B) mixing with H_2O^{18} .

Figure S9 Photocatalytic activity in the presence of TEOA.

Figure S10 Photocatalytic activity under various pH values.

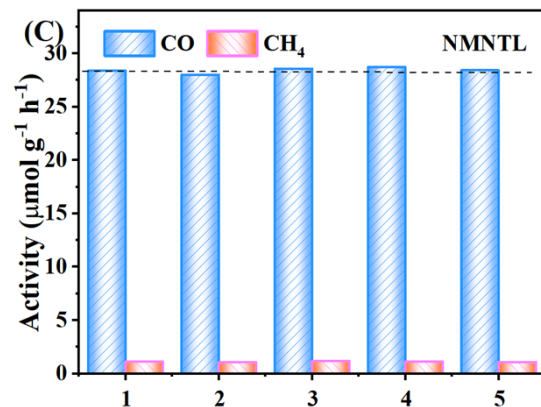


Figure S11 Recycle experiments of (A) NTL, (B) NM and (C) NM₃NTL₁.

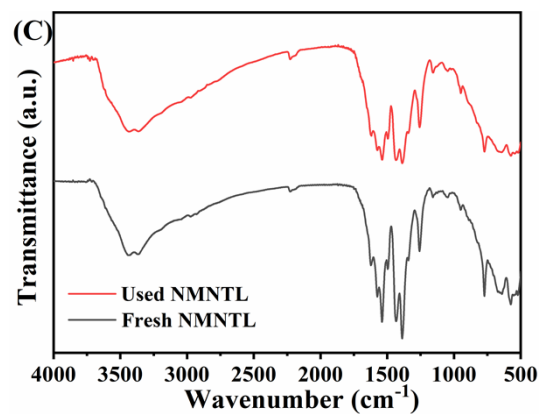


Figure S12 FTIR spectra of fresh and used (A) NTL, (B) NM and (C) NM₃NTL₁.

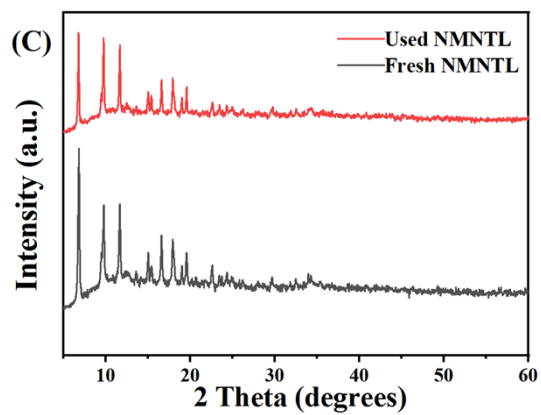


Figure S13 XRD patterns of fresh and used (A) NTL, (B) NM and (C) NM₃NTL₁.

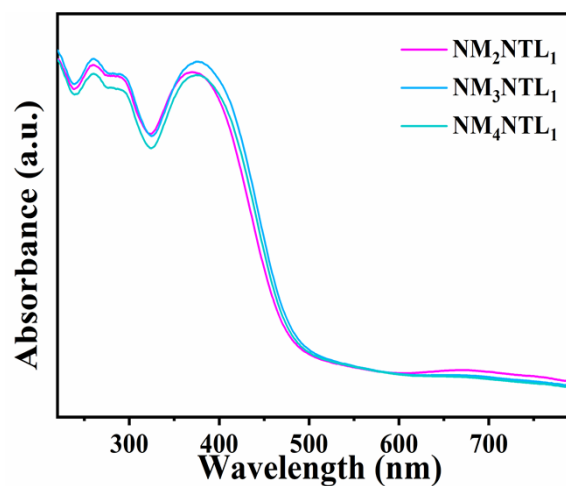


Figure S14 UV-vis DRS spectra of the NM_xNTL_y samples.

Figure S15 Wide scan of XPS spectra.

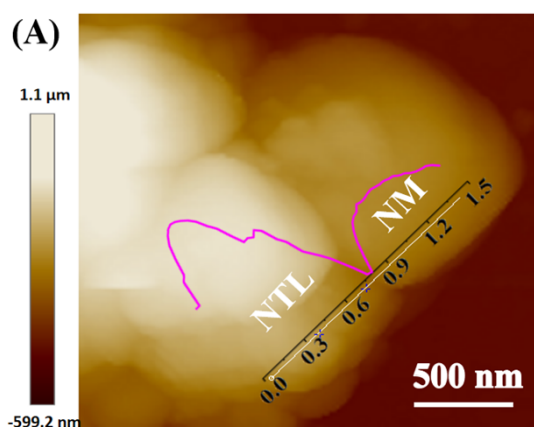


Figure S16 (A) AFM image of NM_3NTL_1 composite; (B) surface potential curves corresponding to the KPFM potential images in Figure 5 (B).

Figure S17 EPR results of (A) $\text{DMPO}\cdot\text{OH}$, (B) $\text{DMPO}\cdot\text{O}_2^-$ for NTL, NM and NMNTL after irradiation for 5 min.

Figure S18 (A) EIS Nyquist plots; (B) Photoluminescence spectra of photocatalysts.

Figure S19 (A) N_2 adsorption-desorption isotherms and (B) the corresponding BJH mesopore size distributions.

Figure S20 TG analysis of (A) NM and (B) NTL.

Figure S21 CO_2 -TPD analysis of NM, NTL and NMNTL.

Figure S22 CO_2 pulse adsorption of as-prepared samples.

Figure S23 In situ DRIFTS measurement for NM.

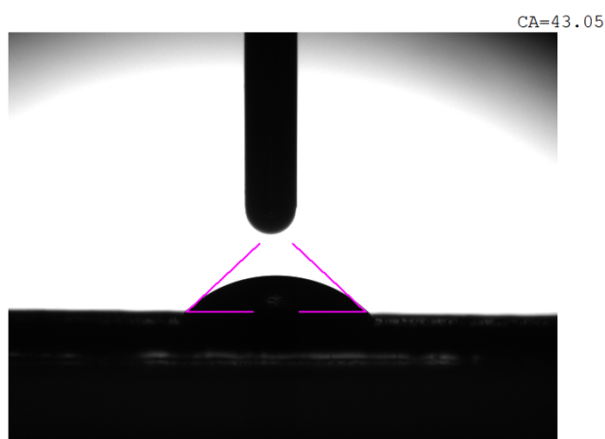


Figure S24 Contact angle for NM with H_2O .

Figure S25 Gas chromatography of reaction gas and the pure CO_2 .

Figure S26 O_2 pulse adsorption of as-prepared samples.

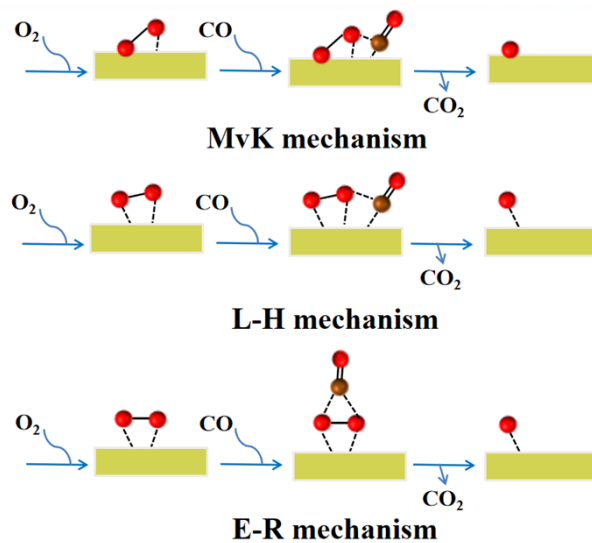


Figure S27 CO oxidation mechanism.

Reference

- [1] Y. Horiuchi, T. Toyao, M. Saito, K. Mochizuki, M. Iwata, H. Higashimura, M. Anpo, M. Matsuoka, *J. Phys. Chem. C*, 2012, **116**, 20848-20853.
- [2] X. M. Cheng, X. Y. Dao, S. Q. Wang, J. Zhao, W. Y. Sun, *ACS Catal.*, 2021, **11**, 650-658.
- [3] X. M. Cheng, Y. M. Gu, X. Y. Zhang, X. Y. Dao, S. Q. Wang, J. Ma, J. Zhao, W. Y. Sun, *Appl. Catal. B-Environ.*, 2021, **298**, 120524.
- [4] R. Ikreedeegh, M. Tahir, J. Environ, *J. Environ. Chem.*, 2021, **9**, 105600.
- [5] S. Y. Chen, X. L. Xu, H. Y. Gao, J. J. Wang, A. Li, X. W. Zhang, *J. Phys. Chem. C*, 2021, **125**, 9200-9209
- [6] G. Wang, C. T. He, R. Huang, J. J. Mao, D. S. Wang, Y. D. Li, *J. Am. Chem. Soc.*, 2020, **142**, 19339-19345.
- [7] X. Y. Zhao, M. Y. Xu, X. H. Song, W. Q. Zhou, X. Liu, Y. Yan, P. W. Huo, *Chem. Eng. J.*, 2022, **437**, 135210.

- [8] R. N. Wang, Z. Y. Qiu, S. P. Wan, Y. N. Wang, Q. Liu, J. Ding, Q. Zhong, *Chem. Eng. J.*, 2022, **427**, 130863.
- [9] Y. F. Zhao, G. B. Chen, T. Bian, C. Zhou, G. I. N. Waterhouse, L. Z. Wu, C. H. Tung, L. J. Smith, D. O'Hare, T. R. Zhang, *Adv. Mater.*, 2015, **27**, 7824.
- [10] K. X. Wang, C. L. Miao, Y. N. Liu, L. Y. Cai, W. Jones, J. X. Fan, D. Q. Li, J. T. Feng, *Appl. Catal. B-Environ.*, 2020, **270**, 118878.
- [11] S. Kumar, M. A. Isaacs, R. Trofimovaite, L. Durndell, C. M. A. Parlett, R. E. Douthwaite, B. Coulson, M. C. R. Cockett, K. Wilson, A. F. Lee, *Appl. Catal. B-Environ.*, 2017, **209**, 394-404.
- [12] Y. Yang, J. J. Wu, T. T. Xiao, Z. Tang, J. Y. Shen, H. J. Li, Y. Zhou, Z. G. Zou, *Appl. Catal. B-Environ.*, 2019, 255, 117771.
- [13] S. Tonda, S. Kumar, M. Bhardwaj, P. Yadav, S. Ogale, *ACS Appl. Mater. Inter.*, 2018, **10**, 2667.
- [14] Z. D. Lin, R. T. Guo, Y. Yuan, X. Y. Ji, L. F. Hong, W. G. Pan, *Appl. Sur. Sci.*, 2021, **567**, 150805.
- [15] Q. R. Shi, X. Y. Zhang, Y. Yang, J. J. Huang, X. L. Fu, T. Y. Wang, X. D. Liu, A. W. Sun, J. H. Ge, J. Y. Shen, Y. Zhou, Z. L. Liu, *J. Energy Chem.*, 2021, **59**, 9.